ACS OMEGA

http://pubs.acs.org/journal/acsodf

Article

Structure and Elastic Properties of an Unsymmetrical Bi-Heterocyclic Azo Compound in the Langmuir Monolayer and Langmuir−Blodgett Film

Ikbal Ahmed, Tanmay Mathur, A. K. M. Maidul Islam,* Jasper R. Plaisier, Pietro Parisse, Sabu Thomas, and Jayanta Kumar Bal*

Cite This: *ACS Omega* 2020, 5, 21538−21549

Read Online

ACCESS | Metrics & More | Article Recommendations | Supporting Information

ABSTRACT: We study the structure and elastic properties of the bi-heterocyclic azo compound at the air−water interface through surface pressure (π)−area (A) isotherm recording followed by transferring them on hydrophilic and hydrophobic Si surfaces by the Langmuir−Blodgett (LB) deposition method. A substantial change in the area/molecule is observed as a function of subphase pH and temperature. Such parameters strongly influence intramolecular interactions within azo molecules and the interactions between azo molecules and water that manifested in higher surface activity at low temperature and high pH, which in turn modifies the elasticity of azo assembly at the air−water interface. A large pH-dependent hysteresis with negative change in entropy, indicating molecular rearrangements, is observed. Molecular assembly formed at the air−water interface is then transferred onto hydrophilic and hydrophobic Si surfaces at two different surface pressures (5 and 30 mN/m) by the LB technique. The structural analysis performed by X-ray reflectivity and atomic force microscopy techniques suggests that the LB films exhibit an abrupt layered structure on hydrophilic Si, whereas an overall rough film is formed on hydrophobic Si. The coverage and compactness of individual layers are found to increase with the deposition pressure (5 to 30 mN/m).

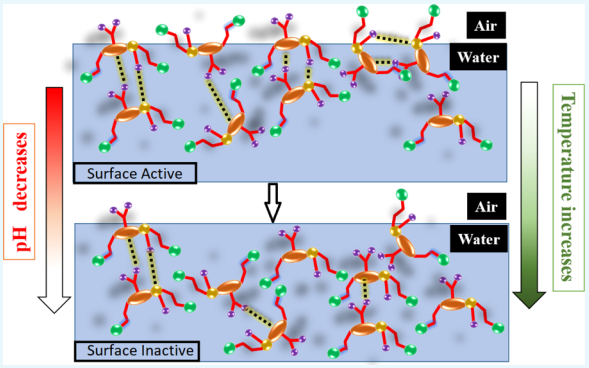

1. INTRODUCTION

Azo−imine function (−N═N−C═N−) can regulate the structural morphology[1] along with their various peculiar properties including light switching,[2,3] multiple isomerisms,[4] photochromic,[5] photo and redox activities,[6,7] and so forth in the azo compounds. Arylazo compounds having the functional group diazenyl R−N═N−R′, in which R and R′ can be either aryl or alkyl, can interact with different types of molecules in a biological cell.[1] The presence of a heterocyclic moiety in the azo compound facilitates in biological activity.[8,9] Generally azo compounds are anionic in nature[10] and pH-sensitive and have ability to bind with the cationic protein and sometimes lipids as well. Researchers have made crucial experiments on controlling azo sizes and shapes, including their surface chemistries using multiple synthesis processes in polar and nonpolar media usually by azo coupling.[11,12] N-heterocyclic and unsymmetrical compounds including pyridine along with adenine and a purine nitrogenous base of nucleic acids are widely used in biological experimentations because of its multimodal applications in self-assembly formation,[13] drug-delivery for in vitro diagnostics,[14−17] bioimaging and biosensing bioprobes[18−23] in tissue and cell analysis for screening micro- and nano-objects and visualization of biological processes.[1,24] Also, their ability to form bioconjugation or biomodification is widely used in cancer diagnosis and therapeutics[1] because of their biocompatible nature in human cells.

Chemicals which seem to be unstable at acidic medium can be treated as unsuitable for future drug industry. In contrast, azo-linked N-heterocyclic compounds are more or less stable in a wide range of pH medium and are also thermodynamically stable in a certain temperature range.[25,26] The biological effectiveness of such N-heterocyclic compounds is enhanced by the inclusion of an azo (−N═N−) group in between these heterocyclic compounds.[9,27] Furthermore, bi-heterocyclic azo compounds have an ability to act as an electron transferring agent[28] and as redox active agent.[29,30] Purine bases have strong affinity for the formation of the H-bond with the effective

Received: May 8, 2020
Accepted: August 7, 2020
Published: August 19, 2020

https://dx.doi.org/10.1021/acsomega.0c02147
ACS Omega 2020, 5, 21538−21549

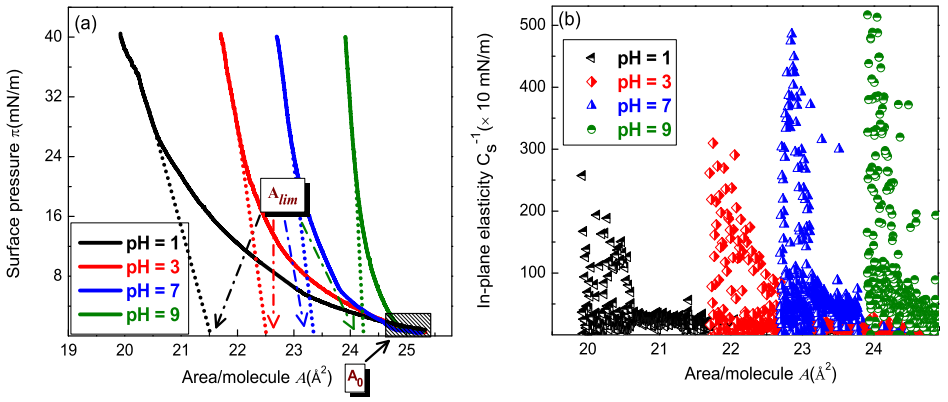

Figure 1. (a) Surface pressure (π)−area (A) isotherm of the azo compound as a function of pH. Dotted line extrapolated to zero pressure axis represents A_{lim}. The shaded box represents the A_0 values. (b) Corresponding in-plane elasticity. All these measurements were carried out at room temperature (RT).

Table 1. Parameters Calculated by Analyzing Surface Pressure (π)−Area (A) Isotherms at Different pHs and Temperatures (T)

subphase parameters		A_0 (Å^2)	A_{lim} (Å^2)	$A_0 - A_{lim}$ (Å^2)	A_c (Å^2)	C_s^{-1} (mN/m)
pH	9	24.8	24.2	0.6	23.95	0−5000
	7	24.9	23.3	1.6	22.86	0−4000
	3	25.0	22.5	2.5	21.75	0−3000
	1	24.8	21.5	3.3	19.92	0−2000
T	20 °C	23.8	22.5	1.3	21.42	0−2000
	15 °C	25.2	23.9	1.2	23.31	0−2200
	10 °C	26.9	25.4	1.5	24.71	0−3000
	5 °C	28.1	27.3	0.8	26.95	0−7000

biomolecules like hormones, metabolites, fatty acids, and so forth. Conjugation of proteins with nitrogen-based compound provides stabilization of the biosystem and induces biocompatibility functions onto this compound for biological interactions and biocoupling.[24,31] Thus, it is cost-effective, environment-friendly, and less toxic in nature; also, less surface passivation or modification is required for the nanoparticle for bioconjugation or other such implications. The presence of such nucleic base containing adenine in the bi-heterocyclic azo compound promoted the compound activity at different pHs, and it can bind with charged and as well as neutral biomolecules very well. Owing to its effectiveness in the medicinal field as a drug for antiviral, antibacterial, and also antifungal purposes, it is essential to know the structural evolution at different conditions mimicking the environment in a human cell. Prior to understanding the interaction of bi-heterocyclic azo compound with different lipids (cholesterol and sphingomyelin) present at human cell membranes, which will be explored in near future, it is essential to know the former molecule very well.

Here, we address the structural modifications of such an azo compound occuring at the air−water interface because of the alteration in pH and temperature of water through analyzing surface pressure−area (π−A) isotherms. This study is performed with specific accent on how different subphase conditions (pH and temperature) can modify the packing and ordering of the azo compound. For better understanding the effects, we calculated various elastic and thermodynamic properties as a function of physicochemical and thermodynamic parameters, such as pH/alkalinity and temperature, respectively. To the best of our knowledge, these properties have never been reported so far especially on this type of rarely found azo compound. In addition, the structure of such rarely[32] found azo molecules in monolayer to multilayer stacking on solid substrates is determined using two complementary techniques, such as X-ray reflectivity (XRR) and atomic force microscopy (AFM).

2. RESULTS AND DISCUSSION

2.1. Monolayer Characteristics. *2.1.1. Surface Pressure−Area Isotherm at Different pHs.* The surface pressure (π)−area (A) isotherm of the azo compound (Figure 1a) at a pH = 7 shows a monotonous increment in surface pressure with decreasing area/molecule. The area/molecule and stiffness of the isotherms systematically decrease with an increase in acidity, that is, lowering the pH value. Contrary to this, at a higher pH value (i.e., pH = 9), that is, in the alkaline environment, the isotherm becomes steeper, and interestingly, the area/molecule increased drastically. These isotherm measurements were performed at ambient conditions. The limiting area (A_{lim}), calculated from the isotherm (tabulated in Table 1) curve by extending the linear condensed part to zero surface pressure axis, is found to be around 24.2, 23.3, 22.5, and 21.5 Å^2/molecule at pH = 9, 7, 3, and 1, respectively. It determines the area/molecule when the Langmuir film undergoes a transition from the liquid phase to the close-packed condensed phase. Their corresponding area of condensation threshold or lift-off area (A_0) (given in Table 1), where surface pressure begins to increase from zero, is obtained around 24.8, 24.9, 25.0, and 24.8 Å^2/molecule, respectively. The lift-off area defines the value of the area at which the transition from the gas phase to liquid phase occurs. In gaseous phase, the molecules stay well apart from each other at the air−water interface and they exert very little (almost

https://dx.doi.org/10.1021/acsomega.0c02147
ACS Omega 2020, 5, 21538−21549

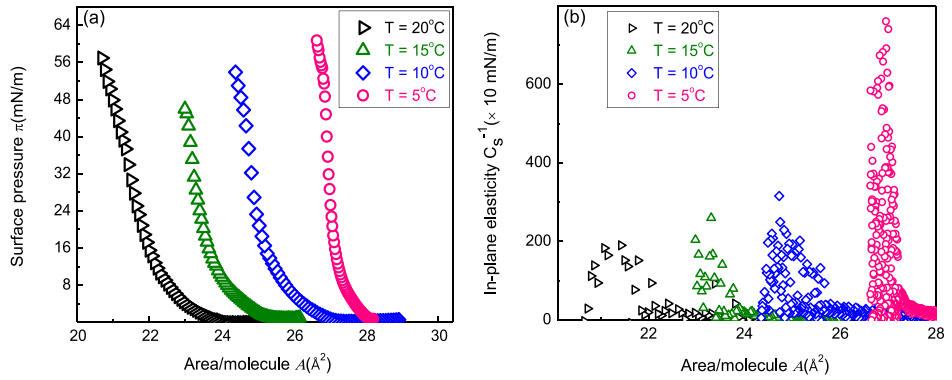

Figure 2. (a) Surface pressure (π)−area (A) isotherm of the azo compound as a function of temperature, (b) corresponding in-plane elasticity. These isotherms were collected at fixed pH of Milli-Q water (pH ≈ 6.1) at RT.

negligible) force. Upon compression, those molecules come closer and start interacting each other that manifested in a hike of surface pressure as evident in the isotherm curves. Thus, physically A_0 marks the onset of intramolecular interactions. Similar A_0 values at different pHs suggest no influence when the molecules are far apart at the air−water interface. On the contrary, a drastic difference in A_{lim} as a function of subphase pH is observed. Notably, all the isotherms were recorded keeping the spreading volume (750 μL) and the concentration (1 g/L) of solutions constant. Therefore, the deviation in A_{lim} values can be attributed to the difference in pH of subphase water. High pH leads to higher surface activity of azo molecules as more number of molecules reaches to the air−water interface contributing in surface pressure. Based on these observations, it is clear that the azo molecules become less compact at air−water interface in acidic environment, whereas at a basic environment, the molecules become less fluidic or more compact. Hence, pH of the subphase alters the interactions within azo molecules and with subphase water. Accordingly, the orientation and packing of the monolayer at air−water interface modify. Interestingly, the difference between A_0 and A_{lim}, that is, (A_0 − A_{lim}), tabulated in the Table 1, increases with the decrement of pH. This quantity actually determines the range of the intermediate liquid phase which becomes wider with the lowering of pH. Consequently, the molecular assembly is found more compressible at lower pH.

A further analysis of isotherms provides compressional modulus (C_s^{-1}) and plotted it as a function of area/molecule (shown in Figure 1b). To extract the information of elastic properties of the monolayers, the reciprocal of monolayer compressibility (C_s), that is, the compressional modulus (C_s^{-1}, also known as in-plane elasticity) was calculated from the isotherms of the azo-containing monolayer at the air−water interface using the following expression[33,34]

$$C_s^{-1} = -A(\partial\pi/\partial A)_T \quad (1)$$

where A is the area per molecule. Numerical value of C_s^{-1}, tabulated in Table 1, increases when the monolayer attains its condensed state. For high acidic medium (pH = 1), the C_s^{-1} value varies between 0 and 2000 mN/m, whereas in high basic medium (pH = 9), C_s^{-1} lies between 0 and 5000 mN/m. Thus, the C_s^{-1} value is found to decrease with the increase in acidity of the subphase. C_s^{-1} curves attain its highest value at certain area/molecule labelled as critical area/molecule A_c. At this position, the maximum increment in surface pressure occurs upon minimum decrement in area/molecule. Physically, it corresponds to the state when the floating Langmuir film reaches its utmost compact structure. Further compression below A_c, the film may cause collapse in the film.

2.1.2. Surface Pressure−Area Isotherm at Different Temperatures. Isotherms were also recorded at four different temperatures, that is, at T = 20, 15, 10, and 5 °C of subphase water (Milli-Q water, pH ≈ 6.1), as depicted in Figure 2a. At relatively higher temperature, the area/molecule and, more importantly, the compressional modulus (C_s^{-1}) (shown in Figure 2b) attain the lowest value (given in Table 1). It indicates that the surface pressure increases slowly upon compression of barriers. The isotherms and numerical values of C_s^{-1} follow a trend of increasing gradually with decreasing temperature. Please note that the low-temperature measurements were done first followed by higher temperature measurements. At each temperature, the isotherm study was made on freshly spread azo molecular layer not on the same layer because of existence of hysteresis.

It is to be noted that our azo compound[27] consists of adenine and pyridine groups (detail structure is given in the Materials and Methods section) with effective π-conjugations, where both N-heterocyclic compounds adenine and pyridine are known to create an acid−base adduct with Brønsted acid via H-bond formation.[35] Adenine has stronger probability to form H-bonding[36] with water as compared to pyridine.[37] As we decrease pH of the water subphase, number of H^+ ions increases in water. Hence, at low pH, the azo molecules form more H-bonds and tend to reside under subphase water, which manifested in low values of A_0, A_{lim}, and C_s^{-1}. Solubility of such bi-heterocyclic azo compounds in water increases with rising temperature. Herskovits and Harrington reported that the solubility of adenine (main constituent of the azo compound) in water increases with the increase of temperature.[38] Here, a nonlinear increment is encountered (see Supporting Information S1).

By extrapolating the curve, the solubility value is extracted at the desired temperatures. At T = 5, 10, 15, 20, and 30 °C the solubility is found to be 15.1, 29.1, 45.0, 58.1, and 91.0 mol L^{-1}, respectively. Therefore, at T = 5 °C, the solubility of the azo compound is expected to be less than at 20 °C. Consequently, at high temperatures because of increased solubility, a less condensed monolayer with a decreased value of area/molecule (A_0, A_{lim}) and C_s^{-1} are obtained. This surface activity study with increasing temperature reveals that the activity of the said compound decreases. The molecularly

https://dx.doi.org/10.1021/acsomega.0c02147
ACS Omega 2020, 5, 21538−21549

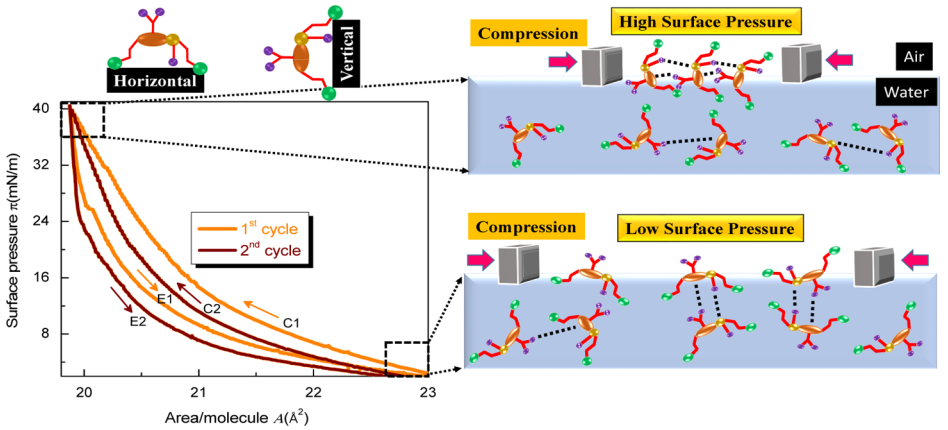

Figure 3. Hysteresis study (compression−expansion of two cycles) of the azo compound at RT (left panel). C1 and E1 represent first cycle compression and expansion, respectively. C2 and E2 represent second cycle compression and expansion, respectively. Schematic depicts organization of molecules at the air−water interface at low and high surface pressures (right panel). At low and high pressures, the molecules are likely to be oriented parallel (horizontal conformation) and perpendicular (vertical conformation) to the water surface, respectively. The probable interactions are shown by dotted lines (right panel).

associated rigid surface molecule is broken down with rising the temperature because of the escalation of molecular vibration.[39] Hence, some of the H-bonds might be broken down. As a consequence, empty spaces developed between the surface molecules that incites more water molecules to come at the air−water interface. Under these circumstances, some azo molecules may be surrounded by more water molecules and driven into bulk, reducing the number of molecules at the air−water interface. Henceforth, the monolayer occupies less area and exhibits less surface pressure. The effect of the subphase temperature on the molecular organization would be better assessed by monitoring surface pressure keeping the barriers fixed and vary the temperature. At T = 5 °C, barriers were fixed at a position that elevates the surface pressure to 61.83 mN/m. This pressure reduces to 44.65 mN/m gradually (see Supporting Information S2) with the rise in temperature up to 30 °C. Generally, surface tension decreases (or surface pressure increases) with increasing temperature because cohesive forces decrease with an increase of molecular thermal motion. Thus, the reduction in pressure can be attributed to the hopping of molecules from the air−water interface to bulk water because of increased solubility. The isotherms of different pH values (1, 3, 7, and 9) were studied at RT (≈20 °C, environment temperature controlled by AC), and the isotherms of different temperatures (5, 10, 15, and 20 °C, temperature of cold water flowing through the cooling line which is controlled by the chiller) were studied at pH = 6.1. The C_s^{-1} value for the 20 °C (recorded by chiller) (at pH = 6.1) isotherm is 0−2000 mN/m, while that for the pH = 7 (at 20 °C, recorded by AC) isotherm is 0−4000 mN/m and for the pH = 3 (at 20 °C) isotherm is 0−3000 mN/m. The apparent inconsistency in the in-plane elasticity values from two sets of measurements for nearly similar pressure and temperature can be understood considering the fact that flowing of water by chiller in temperature variation measurements might perturb the isotherm characteristics and hence the elasticity. Additionally, a finite temperature gradient from the cooling line to the air−water interface is likely to exist as the water top surface is in contact with RT; therefore, there must be a temperature gradient. Perhaps, the actual temperature at the air−water interface in temperature variation measurement would be higher than what recorded by chiller. This higher temperature can be responsible for decreased elasticity.

2.1.3. Hysteresis Study. The surface pressure−area hysteresis isotherm of the azo compound at the air−water interface is shown in Figure 3. A striking behavior is observed in repetitive compression and expansion isotherm cycles (two cycles). It is evident from Figure 3 that the expansion curves (E1 and E2) follow different trajectories than the route followed by compression curves (C1 and C2). The E1 and E2 isotherms are steeper than those of C1 and C2. According to the steepness, the four curves could be arranged as C1 < C2 < E1 < E2. More interestingly, the steepness of C2 recovers its value to some extent as obtained in the first cycle. It is clear that the repetitive compression−expansion cycles lead to a more compact monolayer structure. Notably, the length (i.e., horizontal conformation) and the breadth (vertical conformation) of the molecule are 1.8 and 1.5 nm, respectively. In the first compression C1 of the monolayer, self-organization of the molecules occur. During the self-organization process, the floating monolayer at the interface exhibits a transformation from horizontal (greater cross-sectional area) to vertical (less cross-sectional area) conformation, as depicted schematically in Figure 3 (right panel). This transition persists to some extent when the barriers move apart but some molecules flip to horizontal conformation having larger area during expansion. Such partial reversibility is revealed when the steepness again decreases during C2. After reaching the same pressure π = 40 mN/m, it drops more abruptly. This implies that the azo assembly progressively takes more compact packing with number of cycles. Notably, the final pressures for the fully expanded azo monolayer after completion of E1 and E2 remain nearly same to the initial pressures of C1 and C2, suggesting no loss of molecules from the air−water interface. Hence, this hysteresis may correspond to the different intermolecular arrangements or conformations in the compression and expansion cycles.

Now, because different degrees of organization must be related to entropy S, the hysteresis of the compression−expansion curves is apparently correlated with an alteration in the entropy ΔS of the monolayer film.[40] According to the entropy law of thermodynamics applied to the isothermal compression−expansion cycle of a monolayer system, the

https://dx.doi.org/10.1021/acsomega.0c02147
ACS Omega 2020, 5, 21538−21549

change in entropy ΔS between the initial A_i and final A_f film areas is

$$\Delta S = S_{exp} - S_{com} = \frac{\Delta W}{T} \quad (2)$$

where $\Delta W = W_{exp} - W_{com}$ is the difference in work done (per mol) between expansion and compression cycles. W_{exp} or W_{com} can be expressed as

$$W_{exp/com} = N_A \int_{A_i}^{A_f} \pi \, dA \quad (3)$$

where N_A is Avogadro's number. The calculated values of W_{exp}, W_{com}, and ΔS are tabulated in Table 2.

Table 2. Parameters Such as Work Done During Compression (W_{com}) and Expansion (W_{exp}) Isotherms and Entropy are Calculated by Analysing of Surface Pressure (π)−Area (A) Hysteresis Isotherms as a Function of No. of Cycles and pH of the Subphase

parameters		W_{com} (kJ/mol)	W_{exp} (kJ/mol)	ΔS (J mol^{-1} K^{-1})
no. of cycles	1	0.27	0.18	−0.31
	2	0.21	0.15	−0.20
pH	9	0.07	0.06	−0.03
	7	0.12	0.10	−0.07
	3	0.21	0.14	−0.23
	1	0.34	0.26	−0.27

The work done during compression is found to be higher than that of expansion, which in turn leads to a negative entropy ΔS change (see Table 2).[41] At the beginning of the isotherm, when lateral pressure is very close to zero, the azo molecules are well separated which in turn leads a flexible disordered orientation at the air−water interface (illustrated schematically in Figure 3, right panel). However, upon compression, when pressure reaches to 40 mN/m, the azo molecules lose freedom as they achieve closely packed assembly having vertical conformation (occupying smaller area as depicted in Figure 3). This result provokes us to continue the hysteresis study at different pHs of the subphase. Figure 4 illustrates the evolution of hysteresis curves as a function of pH. The enclosed areas by compression and expansion isotherms are found to vary significantly with pH.

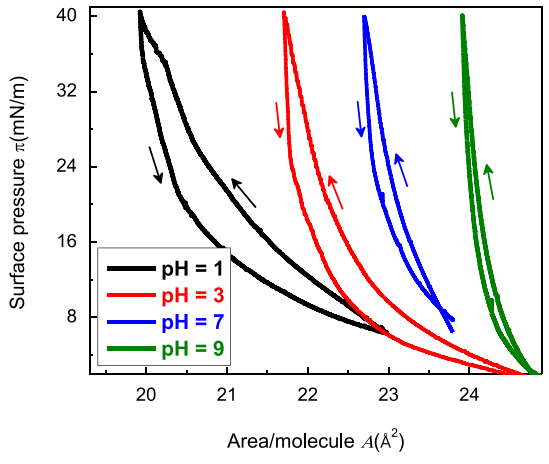

Figure 4. Hysteresis study (compression−decompression) of the azo compound at RT with varying pHs of subphase water.

To shed more light on the quantitative understanding, we have calculated W_{exp}, W_{com}, and ΔS and tabulated in Table 2. Hysteresis is more prevailing when the medium becomes acidic, that is, pH = 1 and 3. A large change in entropy around −0.27 and −0.23 J mol^{-1} K^{-1} is obtained at pH = 1 and 3, respectively. Azo molecules are strongly attracted via ion (H^+)−dipole (−NH_2/−NH group) interaction at pH = 1 and 3 compared to weak dipole−dipole interaction present in neutral (pH = 7) to high pH (pH = 9) conditions. Owing to this strong interaction at low pH, the vertical conformation (shown in Figure 3) formed upon compression is preserved in further expansion resulting in large hysteresis. At high pH, the isotherms are no more compressible (see Figure 4) as the monolayer is highly populated with azo molecules which inhibit any kind of transformation of conformation because of lack of space.

2.2. Structure of Langmuir−Blodgett Films. The conformation of the floating Langmuir monolayer at different compressed phases can be realized by transferring them on suitable substrates. However, the structure of the Langmuir monolayer may change when it is transferred from the air−water interface to a substrate. It involves many variables, such as the materials of the monolayer, the aqueous subphase, the elastic properties of the monolayer, the nature of the substrate, the number of deposited layers, and deposition parameters (pressure, lifting-dipping rate, time of drying between successive depositions, stability of the floating monolayer during the deposition, etc.). However, Langmuir−Blodgett (LB) films of azo molecules were deposited on hydrophilic and hydrophobic Si in one (up), three (up−down−up), and two (down−up) strokes, respectively, at two different surface pressures $\pi \approx 5$ and 30 mN/m. Owing to the polar nature of native oxide,[42] deposition was made in the upstroke (1 and 3 strokes) sequence starting from the bottom of the water subphase. In the case of the hydrophobic substrate, deposition was made in 2 strokes (down−up sequence). All the depositions were done at ambient conditions and at pH ≈ 6.1 (pH of Milli-Q water).

2.2.1. XRR and Electron Density Profile. To probe the structure of these LB films, we performed XRR measurements. As the XRR technique provides an electron density profile (EDP) along the depth, it is possible to find out the structure of LB films. By knowing this structure, one can extrapolate the organization of azo molecules at the air−water interface before transferring on the substrate. XRR data and analyzed curves for LB films deposited on hydrophilic (1 and 3 strokes) and hydrophobic (2 stroke) surfaces at two different surface pressures π = 5 and 30 mN/m are shown in Figure 5. The oscillations obtained from these films show different modulations. However, to get the quantitative information about the structure, all the XRR data were fitted by considering a realistic model structure and corresponding EDPs are given in their insets. For the fitting, all the films are divided into different boxes. Each box carrying constant density and roughness is incorporated at each interfaces. There are three fitting parameters, such as thickness, density, and roughness, for each box. The EDP indicates a drastic density variation along the depth that leads to an overall layered structure in all the LB films. The values of thickness and density of different layer obtained from the EDPs are tabulated in Table 3. The model structure of the films is schematically illustrated in Figure 6. At π = 5 mN/m, films prepared on hydrophilic Si mainly comprised of two layers (bottom and top layers): a

https://dx.doi.org/10.1021/acsomega.0c02147
ACS Omega 2020, 5, 21538−21549

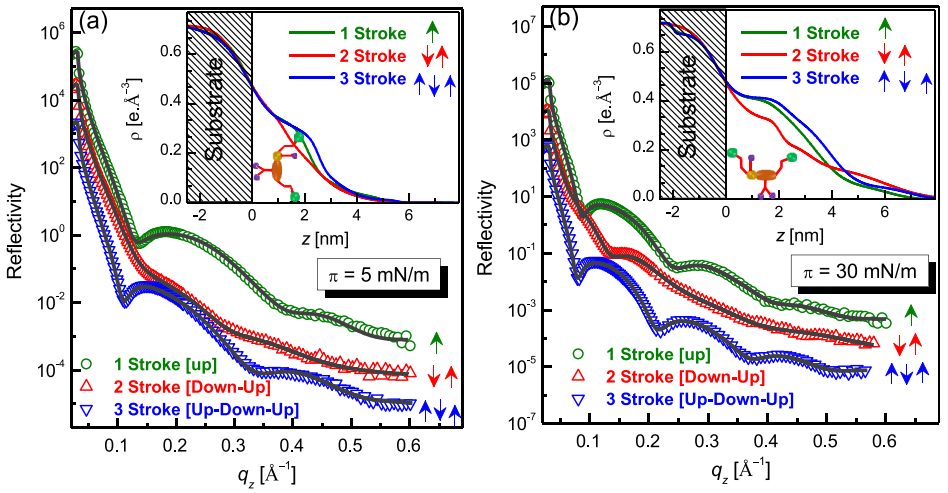

Figure 5. XRR data (different symbols) and analyzed curves (solid line) of azo LB films on hydrophilic (1 stroke [up] and 3 stroke [up−down−up]) and the hydrophobic (2 stroke [down−up]) Si(100) substrate, deposited at surface pressure (a) π = 5 mN/m and (b) π = 30 mN/m (curves are shifted vertically for clarity). Inset: corresponding EDPs. The bottom layer (labelled from z = 0 position to the intercept of vertical dotted line with z axis) is comprised of azo molecules having horizontal (at π = 5 mN/m) and vertical (at π = 30 mN/m) conformations as depicted in the EDPs.

Table 3. Parameters, Such as Thickness (L) and Electron Density (ρ) of the Constituent Layer of Different Films Deposited on Hydrophilic and Hydrophobic Si Obtained from XRR Analysis (i.e., EDP) Assuming a Model Structure[a]

LB films				bottom layer		middle layer		top layer	
deposition pressure	substrate nature	no. of stroke	transfer ratio (TR)	L_{bot} (nm)	ρ_{bot} ($e^-/Å^3$)	L_{mid} (nm)	ρ_{mid} ($e^-/Å^3$)	L_{top} (nm)	ρ_{top} ($e^-/Å^3$)
π = 5 (mN/m)	hydrophilic	1s	↑0.81	1.94	0.32			2.77	0.02
		3s	↑0.85	2.37	0.32			2.60	0.03
			↓0.04						
			↑0.00						
	hydrophobic	2s	↓0.40	1.55	0.32			2.45	0.03
			↑0.00						
π = 30 (mN/m)	hydrophilic	1s	↑0.91	2.23	0.40	1.60	0.21	2.3	0.04
		3s	↑0.93	2.66	0.40	1.52	0.25	2.66	0.05
			↓0.42						
			↑0.26						
	hydrophobic	2s	↓0.55	1.94	0.32	1.55	0.19	3.11	0.11
			↑0.20						

[a]Transfer ratio (TR) obtained at different no. of strokes that is first stroke (up ↑), second stroke (down ↓), and third stroke (up ↑).

highly dense bottom layer (ρ_{bot} = 0.32 $e^-/Å^3$ in 1-stroke and 3-stroke film) and a very low dense top layer (ρ_{top} = 0.02 and 0.03 $e^-/Å^3$ in 1-stroke and 3-stroke film, respectively) (shown in Figure 6). On the contrary, the oscillation of the LB film deposited on hydrophobic Si almost disappears which implies that the film is rough.

Whereas at π = 30 mN/m, the density variation is found to be more abrupt which makes XRR oscillation more prominent (see Figure 5b). They exhibit a three-layered structure (see Figure 6). The density of the bottom layer (ρ_{bot} = 0.40 $e^-/Å^3$) is higher than that of the middle layer (ρ_{mid} = 0.25 $e^-/Å^3$) and density of middle is much higher than the top layer (ρ_{top} = 0.05 $e^-/Å^3$) ($\rho_{bot} > \rho_{mid} > \rho_{top}$). Furthermore, those films deposited at π = 30 mN/m possess higher densities compared to those prepared at π = 5 mN/m. The oscillation and EDP of the film deposited on hydrophobic Si differed drastically from that of hydrophilic substrates. For detail comparison, these parameters are extracted from EDP and tabulated in Table 3. At high pressure (π = 30 mN/m), largely populated azo molecules at the air−water interface may flip and form multilayer during transfer onto the substrate. Hence, a distinct layered structure (not evident in the case of the film deposited on hydrophobic Si) is developed on hydrophilic Si. Interestingly, the thickness of the bottom layer (labelled as L_{bot}, tabulated in Table 3 and shown in Figure 6) is found less for the films prepared at π = 5 mN/m than those prepared at π = 30 mN/m. The thickness of the bottom layer is found to be around 1.55−2.37 and 1.94−2.66 nm at π = 5 and 30 mN/m, respectively. Therefore, the difference in thickness is found to be around 2.9−3.9 Å, which can be correlated with the change in conformation of molecule as its length is 3.0 Å greater than the breadth. Although the dimension of the molecules (length ≈ 18 Å, breadth ≈ 15 Å and height ≈ 1.5 Å) is little less than thickness of the each layer thickness. This may be because of the fluctuation of the molecular assembly on the substrate surfaces. Please note that before XRR analysis, we have estimated the mass density (ρ_v) of such a rare azo compound from its molecular weight and single-molecule dimensions. The mass density is obtained around 1.41 g/cm^3. Then, this density is directly converted to the electron density (ρ_e) using the relation $\rho_v = 3.085\rho_e$.[43] Hence, the bulk electron density of the reported azo compound would be around 0.457 $e^-/Å^3$. This calculated

https://dx.doi.org/10.1021/acsomega.0c02147
ACS Omega 2020, 5, 21538−21549

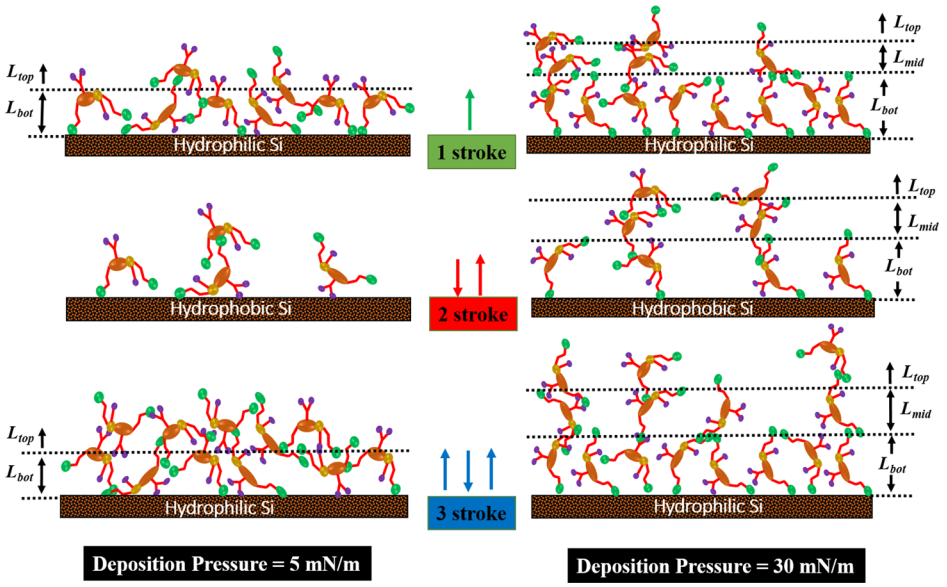

Figure 6. Schematic presentation of LB films formed on hydrophilic (1 and 3 strokes) and hydrophobic (2 strokes) Si at deposition pressure π = 5 and 30 mN/m.

value seems to be convincing as it lies in between the densities of the adenine (0.519 $e^-/Å^3$) and pyridine (0.318 $e^-/Å^3$) which constitute this azo molecule.

The structure of such LB films has been correlated with a TR (given in Table 3) obtained at different number of strokes. The high TR value during the first stroke and the low value in further strokes inhibit the formation of multilayers at low surface pressure (π = 5 mN/m). Hence, a highly dense bottom layer (expected to form in the first stroke) and a very low dense top layer (expected to form in second and/or third strokes) are obtained. In contrary, at high surface pressure (π = 30 mN/m), TR is found to be significant in second and third strokes along with the first stroke which manifested in the multilayer structure. The TR during each stroke at high pressure is greater compared to that at low pressure as molecules are more closely packed at former condition.

In order to understand the transfer of molecules from the air−water interface to substrate surface in different number of strokes at a particular pressure, the transfer amount (TA) is calculated from the data available in the Table 3. At π = 5 mN/m, the total TA is obtained ≈6.8 $e^-/Å^2$ for 1s (one upstroke) and ≈8.4 $e^-/Å^2$ for 3s (up−down−up strokes). Hence, a TA value of 1.6 $e^-/Å^2$, which is nearly 23% with respect to the TA in the first stroke, occurred in successive second (down) plus third (up) stroke depositions. On the other hand, at π = 30 mN/m, the total TA is achieved ≈13.2 $e^-/Å^2$ for 1s (one upstroke) and 15.8 $e^-/Å^2$ for 3s (up−down−up strokes). Therefore, around 20% difference in TA is observed that is caused because of the additional transfer of molecules on the substrate during second (down) and third (up) stroke of deposition. Interestingly, if we look into the TR values (0.42 and 0.26 in second and third stroke, respectively), one should expect a better TA for the 3s film. The TR value of 0.91 in 1s gives rise to a TA of 13.2 $e^-/Å^2$. Hence, the TR values 0.42 and 0.26 recorded in second and third strokes correspond to the TA ≈ 6.1 and 3.8 $e^-/Å^2$, respectively. Thus, a total TA of 9.9 $e^-/Å^2$ (i.e., 75% with respect to the TA in the first stroke) should have been deposited in further down (second) and up (third) strokes, but it is not the case. Rather a huge discrepancy between the calculated TA and the amount predicted by TR values is noticed. This deviation could be realized by considering the fact that some of the molecules may dissolve during complete immersion into the subphase in the second (i.e., down) stroke before starting the third stroke. Perhaps, this certain amount of dissolution of molecules, which were transferred during the second stroke, inhibits the improvement in TA in multilayer depositions. However, a drastic improvement (≈88−94%) in TA of corresponding strokes is encountered because of rise of surface pressure from 5 to 30 mN/m. Please note that the 1s and 3s films are two separate films, and we are assuming that the same amount of molecules (same TA) is transferred in the 1s film and in the first stroke of the 3s film. Despite the fact that all the parameters were kept same and the depositions were done simultaneously, there might be some small differences because of sample-to-sample uncertainty in experiments.

It is also clear that for π = 5 mN/m, a very small fraction of bilayer in addition to the monolayer is formed even in the first stroke itself. Similarly, for π = 30 mN/m, a small fraction of the bilayer and very small fraction of the trilayer in addition to the monolayer (of different orientation) are formed in the first stroke. It is unlikely to form multilayer in one stroke (shown in Figure 6). This can be understood considering the fact that during the transfer of molecules from the water surface onto the solid surface, some molecules may not like to attach with the substrate as they bonded with other molecules which led the formation of middle and top layers in one stroke. However, during this process, there was a continuous supply of molecules and the density of the bottom layer remains good. When the number of strokes increases from 1 to 3, a more thick and smooth film is obtained. It indicates that the additional down−up stroke facilitates the reorganization of azo molecules in forming a better layered structure. Another possibility of multilayer formation on the substrate in the single upstroke would be the intake of the inbuilt multilayered structure of the Langmuir film at the air−water interface. It is very difficult to discard one of them convincingly in the present study as no direct characterization was done at the air−water interface.

https://dx.doi.org/10.1021/acsomega.0c02147
ACS Omega 2020, 5, 21538−21549

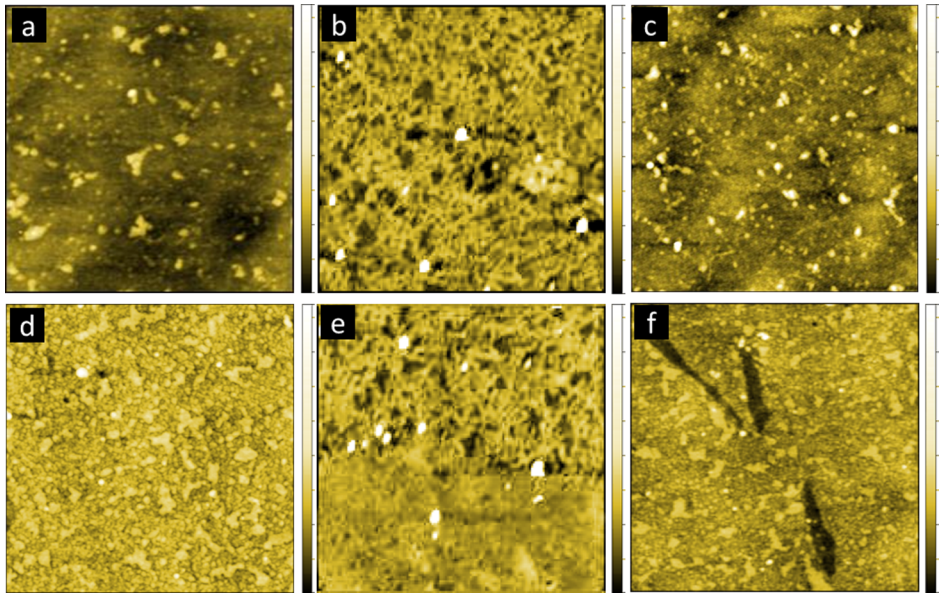

Figure 7. AFM images (scan area = 2 × 2 μm^2) of azo LB films deposited at π = 5 mN/m (a) 1s, (b) 2s, (c) 3s and at π = 30 mN/m, (d) 1s, (e) 2s, and (f) 3s. Their corresponding Z_{max} (maximum value of the height scale) are 6, 8, 8, 10, 10, and 12 nm, and root-mean-square (rms) roughness (σ_{rms}) are 9.0, 17.8, 8.0, 6.3, 14.4, and 7.8 Å, respectively.

However, the existence of the latter model demands more thick films (at least some amounts) (as significant TR values observed in second and third strokes) than what we obtained. Moreover, the hydrophobic substrate exhibits lower TR values than the hydrophilic one which indicates that the azo compound likes to transfer on hydrophilic Si rather likes to reside at the air−water interface. This can be attributed to the dominant hydrophilic nature of azo molecules. Also, the TR value at each stroke fully compliment the obtained EDP for every films.

2.2.2. AFM and Topography. Various layered islands are directly encountered in the surface topography images (shown in Figure 7a−f), although their morphologies are different on polar and nonpolar surfaces. However, these morphologies do not alter appreciably with number of strokes (1 and 3) on hydrophilic Si which is also expected from the XRR analysis. The basic difference between the structure on hydrophilic and hydrophobic surfaces is that the former surface exhibits a small island structure on top of a very compact layer (see Figure 7a,c). The average height of these islands is found to vary in the range of 2.5−6 nm. These islands correspond to the top layer on a highly dense bottom layer as labelled in the EDP. In contrast, the EDP (see Table 3) suggests that the thickness of the top layer varies from 2.45 to 2.74 nm. Higher thickness of the top layer obtained in AFM appears as roughness in EDP. The coverage (surface area) of the top layer on hydrophilic Si extracted from AFM is found nearly equal to 15−20% (estimated error ≈ 5%). Their coverage can also be estimated from EDP. Considering the maximum density 0.4 $e^-/Å^3$ of the bottom layer as 100%, the coverage of the top layer for all the films (except hydrophobic films) would vary in the range of 10−20% (±10%). Hence, AFM results are in agreement with the XRR analysis. Nevertheless, coverage of the films or layers is calculated by marking grains above a threshold height using Gwyddion software. However, the morphology differs drastically when the depositions are done at high pressure, that is, at π = 30 mN/m (see Figure 7). A layered structure is more evident on hydrophilic Si (see Figure 7d,f), whereas such distinct layering is absent on hydrophobic surfaces (Figure 7b,e). Different layers are evident in LB films deposited on hydrophilic Si in three strokes (see Figure 7f).

3. CONCLUSIONS

In conclusion, we have demonstrated that the elastic properties of the bi-heterocyclic azo compound, which is the constituent of biological molecule like adenine, is found to evolve drastically at the air−water interface as a function of subphase pH and temperature. High pH and low temperature appear to move the isotherms to a large area/molecule because of improved solvation of the azo compound in the subphase. Consequently, the elasticity of such azo assembly, as deduced from the steepness of the isotherm curve, goes down with pH reduction and temperature elevation. A strong pH-responsive hysteretic feature accompanied with a negative change in entropy may involve transition from horizontal (larger occupied area) conformation to vertical (smaller occupied area). This can be envisioned as an acidic subphase (lower pH) that facilitates in-plane interaction between azo molecules via H-bond formation resulting in large hysteresis. The partial reversibility of successive hysteresis cycles leads to a more condensed phase progressively. The structural analysis of such molecular assembly upon transferring on hydrophilic and hydrophobic Si surfaces at two different surface pressures (π = 5 and 30 mN/m) reveals that a layered structure is formed on hydrophilic Si. On the contrary, this layered structure is likely to disappear on hydrophobic Si, rather a less covered rough film is formed. The layering becomes more pronounced at higher deposition pressure (π = 30 mN/m), when the assembly is more compact. Multilayer films with partially covered top layers are obtained. The structure of solid-supported films at various conditions is important to replicate the organization or conformation of the predeposited films at the air−water interface which essentially have insinuations in the biological applications of human body. In particular, the consequences of this study would be advantageous to understand the interaction of this azo compound with different

https://dx.doi.org/10.1021/acsomega.0c02147
ACS Omega 2020, 5, 21538−21549

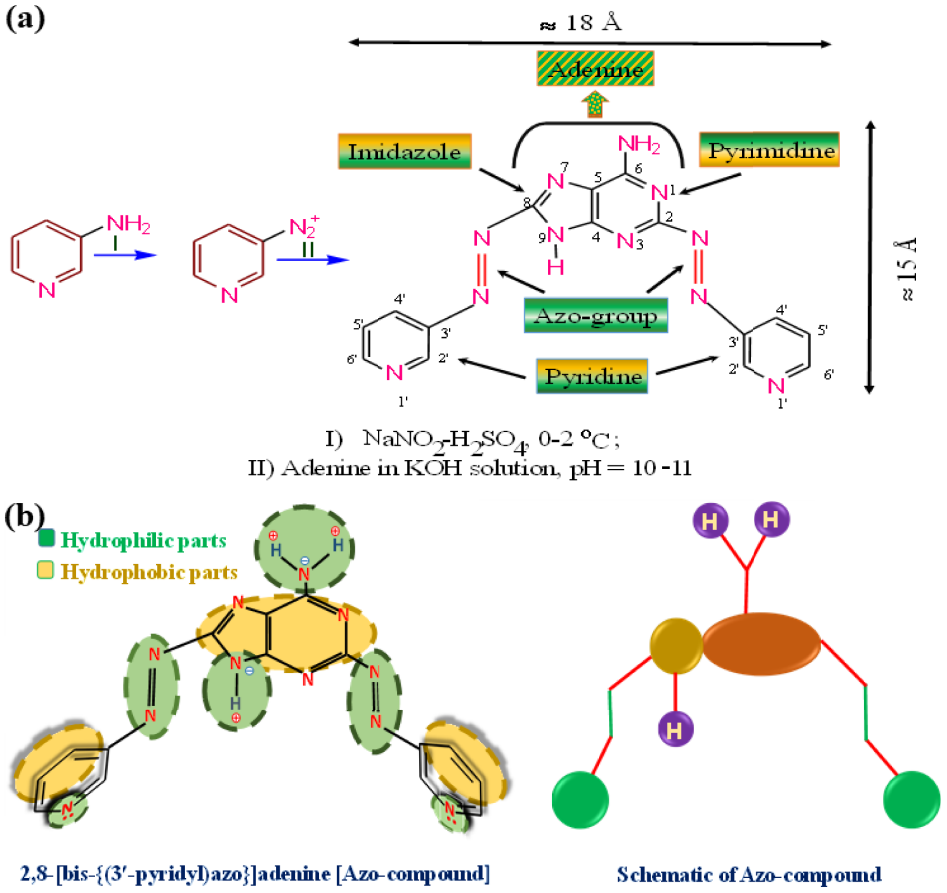

Figure 8. (a) Synthesis steps of the azo compound and (b) different parts (hydrophilic and hydrophobic) of the compound and its pictorial representation.

biomolecules, such as sphingomyelin, cholesterol, and bovine serum albumin, present in the human body cell membrane.

4. MATERIALS AND METHODS

4.1. Materials. The detailed synthesis procedure of our azo compound, IUPAC name 2,8-[bis-{(3′-pyridyl)azo}]adenine, (M_w = 345 g/mol) is described elsewhere.[27] In brief, the diazotization process was carried out by the slow addition of aqueous solution of $NaNO_2$ (0.75 g) into the mixture of 10 mL dilute H_2SO_4 (1:1) and 3-aminopyridine (1 g, 10.6 mmol) until the solution color reached yellow at 0−2 °C. The solution mixture was kept for 2−3 min. Then, the cold yellow color solution of pyridine−diazonium salt was added dropwise into the cold aqueous solution mixture of adenine (1.45 g, 10.7 mmol) and potassium hydroxide (2 g) with constant stirring and finally obtained an orange-red precipitate. After 4 h, the precipitate was filtered, washed with little water, and kept into desiccators. Then, the compound was dissolved in dilute HCl, neutralized with the solid $NaHCO_3$, filtered, washed with little water, and finally dried. The crude compound was purified by the column chromatographic method, and finally, a red compound was isolated by using methanol as mobile solvent. A brief description of the steps involved in the synthesis and a tentative idea of its dimension are shown in the Figure 8a. This molecule shows amphiphilic nature as both hydrophilic and hydrophobic parts being present (schematically shown in Figure 8b).

4.2. Preparation of Langmuir Monolayer and Film Deposition. For the study and fabrication of Langmuir monolayers and LB films, a commercial LB instrument (Apex Instruments, model no.: LBXD-NT) having a PTTE trough (560 mm length, 200 mm width, and 5 mm height) and two software-controlled barriers located at the interface were employed. The LB deposition well has a dimension of 60 mm (length), 200 mm (width), and 60 mm (height). The surface pressure of the isotherms were measured by means of the Wilhelmy plate method with an accuracy of ±0.01 mN/m. Here, a strip of filter paper (dimensions = 10 × 25 mm^2) in contact with the aqueous subphase was incorporated. Prior to start of the experiments, ultrahigh pure Milli-Q water and ethanol were used to clean the LB trough repeatedly. A solution of the azo compound having a concentration of 1 g/L is prepared using methanol solvent and kept for 24 h for homogeneous dissolution. To record the isotherm of the azo compound, it was carefully spread all over the subphase Milli-Q water drop by drop with a Hamilton microsyringe having a precision of 2.5 μL. The solution was left for 15−20 min for the evaporation of the solvent and was allowed to reach an equilibrium surface pressure. Afterward, the monolayer was compressed with two movable barriers on the water surface at a speed of 8 mm/min to record the surface pressure−area (π−A) isotherms. The isotherms were recorded for multiple pH values (pH = 1, 3, 7, and 9) and different temperatures (T = 5, 10, 15, and 20 °C) of water following the aforementioned procedure. The pH of subphase water was changed using NaOH and HCl, whereas temperature of subphase water was controlled using a chiller (Firstsource Company) equipped with LB trough. The cooling line, that is, the inlet and outlet

https://dx.doi.org/10.1021/acsomega.0c02147
ACS Omega 2020, 5, 21538−21549

port by which cold water circulates is located under the trough. The temperature variation measurements were performed by connecting a chiller with the LB trough, whereas the isotherms observed at different pHs were taken at RT without connecting the chiller as the flowing of cold water through the cooling line might perturb the isotherm. The fabrication of the LB monolayer and multilayer films on hydrophilic and hydrophobic Si(100) substrates were performed at two constant pressures, that is, at 5 and 30 mN/m by maintaining a fixed barrier compression and expansion speed of 8 mm/min. Moreover, the lifting and dipping of substrates through the subphase were fixed at a speed of 5 mm/min. After deposition, the films were left for 10 min above the subphase for natural drying before their collection.

Before LB deposition, some substrates were made hydrophilic by RCA cleaning and some were made hydrophobic by hydrofluoric (HF) treatment.[44] In RCA cleaning, the Si surfaces (of size $\approx 25 \times 15$ mm^2) were made hydrophilic by introducing the hydroxyl group (−OH) after boiling them in a mixture of ammonium hydroxide (NH_4OH, Sigma-Aldrich, 25%), hydrogen peroxide (H_2O_2, Acros Organics, 39%), and Milli-Q water ($H_2O/NH_4OH/H_2O_2$ = 2:1:1, by volume) for 10 min at 100 °C. The RCA-cleaned hydrophilic substrates were made hydrophobic by HF acid treatment. Here, the RCA-cleaned Si was vertically immersed into HF (10%, 20 mL) solution for 3 min, and afterward, the substrates were washed in Milli-Q and dried prior to film deposition. The quality of hydrophilicity and hydrophobicity were tested by water contact angle measurements which yield ∼14 and 79°, respectively.

4.3. Characterization. XRR measurements were carried out at the beamline MCX[45] at Elettra-Sincrotrone Trieste. The wavelength used was 1.54 Å. The beamline is equipped with a high resolution four-circle diffractometer and a three (X, Y, and Z) translational stage. Scattered intensities were recorded using a scintillator detector behind a set of receiving slits. Data were taken in specular condition, that is, the incident angle is equal to the reflected angle and both are in a scattering plane. Under such conditions, a nonvanishing wave vector component, q_z, is given by $(4\pi/\lambda)\sin\theta$ with a resolution of 0.001 Å^{-1}. The XRR technique essentially provides an EDP, that is, in-plane (x−y) average electron density (ρ) as a function of depth (z) in high resolution.[46] From EDP, it is possible to estimate film thickness, electron density, and interfacial roughness.[46,47] Analysis of XRR data has been carried out using the matrix technique.[46,48] In general, the electron-density variation in a specimen is determined by assuming a model and comparing the simulated profile with the experimental data. EDP is extracted from the fitting of experimental XRR data. For the analysis, each film has been divided into a number of layers including roughness at each interface.[46,47] An instrumental resolution in the form of a Gaussian function and a constant background were also included at the time of data analysis.

Surface morphology of the films were collected by an AFM (NT-MDT), and scans were performed over several portions of the films for different scan areas after completion of XRR measurements. AFM images were collected in the noncontact mode using the silicon cantilever (dimensions: 125 μm × 30 μm, spring constant = 42 N/m, resonance frequency = 320 kHz) and sharp needle-like tip in ambient conditions to minimize the tip-induced modification of the sample surface. Gwyddion software was used for image processing and analysis. A contact angle measurement setup (Acam-MSC) was used to measure the contact angle of water on RCA- and HF-cleaned Si surfaces.

■ ASSOCIATED CONTENT

Supporting Information

The Supporting Information is available free of charge at https://pubs.acs.org/doi/10.1021/acsomega.0c02147.

Solubility of adenine (main constituent of our azo compound) in water as a function of temperature and evolution of surface pressure with temperature keeping barrier position fixed (PDF)

■ AUTHOR INFORMATION

Corresponding Authors

A. K. M. Maidul Islam − *Department of Physics, Aliah University, Newtown, Kolkata 700156, India*; Email: maidul79@gmail.com

Jayanta Kumar Bal − *Department of Physics, Abhedananda Mahavidyalaya, University of Burdwan, Sainthia, West Bengal 731234, India*; orcid.org/0000-0002-1814-1018; Email: jayanta.bal@gmail.com

Authors

Ikbal Ahmed − *Department of Physics, Aliah University, Newtown, Kolkata 700156, India*; orcid.org/0000-0003-0969-788X

Tanmay Mathur − *Department of Chemistry, Abhedananda Mahavidyalaya, University of Burdwan, Sainthia, West Bengal 731234, India*

Jasper R. Plaisier − *Elettra-Sincrotrone Trieste S.C.p.A., 34149 Trieste, Italy*

Pietro Parisse − *Elettra-Sincrotrone Trieste S.C.p.A., 34149 Trieste, Italy*

Sabu Thomas − *International and Inter University Centre for Nanoscience and Nanotechnology, Mahatma Gandhi University, 686560 Kottayam, India*; orcid.org/0000-0003-4726-5746

Complete contact information is available at: https://pubs.acs.org/10.1021/acsomega.0c02147

Notes

The authors declare no competing financial interest.

■ ACKNOWLEDGMENTS

J.K.B. gratefully acknowledges Department of Science and Technology (DST), Government of India, for providing the research grant through SERB (CRG/2018/002290) and INSPIRE Faculty Award (IFA13-PH-79). The financial support received from the DST and ICTP under the India-Elettra access program to carry out XRR experiments at MCX beamline of Elettra is gratefully acknowledged.

■ REFERENCES

(1) Sahoo, J.; Paidesetty, S. K. Medicinal Interest of AZO-Based Organic Compounds: A Review. *Asian J. Pharm. Clin. Res.* **2016**, *9*, 33−39.

(2) Otsuki, J.; Omokawa, N.; Yoshiba, K.; Yoshikawa, I.; Akasaka, T.; Suenobu, T.; Takido, T.; Araki, K.; Fukuzumi, S. Synthesis and Structural, Electrochemical, and Optical Properties of Ru(II) Complexes with Azobis(2,2′-Bipyridine)S. *Inorg. Chem.* **2003**, *42*, 3057−3066.

(3) Crespi, S.; Simeth, N. A.; König, B. Heteroaryl Azo Dyes as Molecular Photoswitches. *Nat. Rev. Chem.* **2019**, *3*, 133−146.

(4) Kaim, W. Complexes with 2,2′-Azobispyridine and Related 'S-Frame' Bridging Ligands Containing the Azo Function. *Coord. Chem. Rev.* **2001**, *219−221*, 463−488.
(5) Yam, V. W.-W.; Lau, V. C.-Y.; Cheung, K.-K. Synthesis, Photophysics and Photochemistry of Novel Luminescent Rhenium(I) Photoswitchable Materials. *J. Chem. Soc., Chem. Commun.* **1995**, *2*, 259.
(6) He, Y.; Gu, X.; Guo, M.; Wang, X. Dendritic Azo Compounds as a New Type Amorphous Molecular Material with Quick Photo-induced Surface-Relief-Grating Formation Ability. *Opt. Mater.* **2008**, *31*, 18−27.
(7) Luo, C.; Xu, G.-L.; Ji, X.; Hou, S.; Chen, L.; Wang, F.; Jiang, J.; Chen, Z.; Ren, Y.; Amine, K.; Wang, C. Reversible Redox Chemistry of Azo Compounds for Sodium-Ion Batteries. *Angew. Chem., Int. Ed.* **2018**, *57*, 2879−2883.
(8) Keerthi Kumar, C. T.; Keshavayya, J.; Rajesh, T. N.; Peethambar, S. K.; Shoukat Ali, A. R. Synthesis, Characterization, and Biological Activity of 5-Phenyl-1,3,4-Thiadiazole-2-Amine Incorporated Azo Dye Derivatives. *Org. Chem. Int.* **2013**, *2013*, 370626.
(9) Shridhar, A. H.; Keshavayya, J.; Peethambar, S. K.; Joy Hoskeri, H. Synthesis and Biological Activities of Bis Alkyl 1,3,4-Oxadiazole Incorporated Azo Dye Derivatives. *Arabian J. Chem.* **2016**, *9*, S1643−S1648.
(10) Ghosh, B. K.; Chakravorty, A. Electrochemical Studies of Ruthenium Compounds Part I. Ligand Oxidation Levels. *Coord. Chem. Rev.* **1989**, *95*, 239−294.
(11) Patterson, D. Some Factors in Batch and Continuous Coupling Processes Affecting the Particle Size Distribution of Azo Pigments. *Ber. Bunsen-Ges. Phys. Chem.* **1967**, *71*, 270−276.
(12) Szele, I.; Zollinger, H. *Azo Coupling Reactions Structures and Mechanisms*; Springer, 1983; Vol. *112*, pp 1−66.
(13) Paczesny, J.; Binkiewicz, I.; Janczuk, M.; Wybrańska, K.; Richter, Ł.; Hołyst, R. Langmuir and Langmuir−Blodgett Films of Unsymmetrical and Fully Condensed Polyhedral Oligomeric FBalquioxanes (POSS). *J. Phys. Chem. C* **2015**, *119*, 27007−27017.
(14) Butcher, A.; Gregg, A.; Scammells, P. J.; Rose' Meyer, R. B. Effect of a Novel Partial Adenosine A1 Receptor Agonist VCP102 in Reducing Ischemic Damage in the Mouse Heart. *Drug Dev. Res.* **2007**, *68*, 529−537.
(15) Monostori, P.; Klinke, G.; Hauke, J.; Richter, S.; Bierau, J.; Garbade, S. F.; Hoffmann, G. F.; Langhans, C.-D.; Haas, D.; Okun, J. G. Extended Diagnosis of Purine and Pyrimidine Disorders from Urine: LC MS/MS Assay Development and Clinical Validation. *PLoS One* **2019**, *14*, No. e0212458.
(16) Safranow, K. Identification and Quantitation of Purine Derivatives in Urinary Calculi as Markers of Abnormal Purine Metabolism by Using High-Performance Liquid Chromatography (HPLC). *Ann. Acad. Med. Stetin.* **2000**, *46*, 35−49.
(17) Crimi, N.; Polosa, R.; Mistretta, A. Purine Derivatives in the Study of Allergic Inflammation in Respiratory Diseases. *Allergy* **1997**, *52*, 48−54.
(18) Sharma, V.; Jelen, F.; Trnkova, L. Functionalized Solid Electrodes for Electrochemical Biosensing of Purine Nucleobases and Their Analogues: A Review. *Sensors* **2015**, *15*, 1564−1600.
(19) Dopierała, K.; Bojakowska, K.; Karasiewicz, J.; Maciejewski, H.; Prochaska, K. Interfacial Behaviour of Cubic Silsesquioxane and Silica Nanoparticles in Langmuir and Langmuir−Blodgett Films. *RSC Adv.* **2016**, *6*, 94934−94941.
(20) Ghanbari, H.; Cousins, B. G.; Seifalian, A. M. A Nanocage for Nanomedicine: Polyhedral Oligomeric Silsesquioxane (POSS). *Macromol. Rapid Commun.* **2011**, *32*, 1032−1046.
(21) Lipi, F.; Chen, S.; Chakravarthy, M.; Rakesh, S.; Veedu, R. N. In Vitro Evolution of Chemically-Modified Nucleic Acid Aptamers: Pros and Cons, and Comprehensive Selection Strategies. *RNA Biol.* **2016**, *13*, 1232−1245.
(22) Minagawa, H.; Onodera, K.; Fujita, H.; Sakamoto, T.; Akitomi, J.; Kaneko, N.; Shiratori, I.; Kuwahara, M.; Horii, K.; Waga, I. Selection, Characterization and Application of Artificial DNA Aptamer Containing Appended Bases with Sub-Nanomolar Affinity for a Salivary Biomarker. *Sci. Rep.* **2017**, *7*, 42716.
(23) Sallin, O.; Reymond, L.; Gondrand, C.; Raith, F.; Koch, B.; Johnsson, K. Semisynthetic Biosensors for Mapping Cellular Concentrations of Nicotinamide Adenine Dinucleotides. *eLife* **2018**, *7*, No. e32638.
(24) Sivakova, S.; Rowan, S. J. Nucleobases as Supramolecular Motifs. *Chem. Soc. Rev.* **2005**, *34*, 9.
(25) Awale, A. G.; Gholse, S. B.; Utale, P. S. Synthesis, Spectral Properties and Applications of Some Mordant and Disperse Mono Azo Dyes Derived from 2-Amino-1, 3-Benzothiazole. *Res. J. Chem. Sci.* **2013**, *3*, 81−87.
(26) Lewczuk, R.; Książek, M.; Gańczyk-Specjalska, K.; Cieślak, K. Structure and Thermal Properties of 2,2′-Azobis(1H-Imidazole-4,5-Dicarbonitrile)—A Promising Starting Material for a Novel Group of Energetic Compounds. *Molecules* **2020**, *25*, 314.
(27) Mathur, T.; Seal, M.; Chatterjee, S. N. Synthesis, Characterization and Antimicrobial Activity of Unsymmetrical Bi-Heterocyclic-Azo-Compound(3-Pyridyl-Azo-Adenine). *Heterocycl. Lett.* **2017**, *7*, 171−176.
(28) Krause, R. A.; Krause, K. Chemistry of Bipyridyl-like Ligands. Isomeric Complexes of Ruthenium(II) with 2-(Phenylazo)Pyridine. *Inorg. Chem.* **1980**, *19*, 2600−2603.
(29) Goswami, S.; Chakravarty, A. R.; Chakravorty, A. Chemistry of Ruthenium. 2. Synthesis, Structure, and Redox Properties of 2-(Arylazo)Pyridine Complexes. *Inorg. Chem.* **1981**, *20*, 2246−2250.
(30) Goswami, S.; Chakravarty, A. R.; Chakravorty, A. The Ru II (OH2)−Ru IV (O) Couple in a Ruthenium Complex of 2-(Phenylazo)Pyridine : Homogeneous Catalysis of the Oxidation of Water to Dioxygen. *J. Chem. Soc., Chem. Commun.* **1982**, *22*, 1288−1289.
(31) Saenger, W. *Principles of Nucleic Acid Structures*; Springer: New York, 1984.
(32) Mathur, T.; Jasimuddin, S.; Milton, H.; Woollins, J. D.; Sinha, C. First Example of Mixed Azoheterocycles: Structural Studies of Metallo-Macrocycle Ag(I) versus Tetrahedral Cd(II) Complexes of Pyridyl-Azo-Imidazole. *Inorg. Chim. Acta* **2004**, *357*, 3503−3509.
(33) Ahmed, I.; Haque, A.; Bhattacharyya, S.; Patra, P.; Plaisier, J. R.; Perissinotto, F.; Bal, J. K. Vitamin C/Stearic Acid Hybrid Monolayer Adsorption at Air−Water and Air−Solid Interfaces. *ACS Omega* **2018**, *3*, 15789−15798.
(34) Ahmed, I.; Dildar, L.; Haque, A.; Patra, P.; Mukhopadhyay, M.; Hazra, S.; Kulkarni, M.; Thomas, S.; Plaisier, J. R.; Dutta, S. B.; Bal, J. K. Chitosan-Fatty Acid Interaction Mediated Growth of Langmuir Monolayer and Langmuir-Blodgett Films. *J. Colloid Interface Sci.* **2018**, *514*, 433−442.
(35) Watanabe, M.; Sugeta, H.; Iwahashi, H.; Kyogoku, Y.; Kainosho, M. Detection of Proton-Acceptor Sites of Hydrogen Bonding in Adenine · Uracil Base Pairs by the Use of 15N Magnetic Resonance. *Eur. J. Biochem.* **2005**, *117*, 553−558.
(36) Fliegl, H.; Lehtonen, O.; Sundholm, D.; Kaila, V. R. I. Hydrogen-Bond Strengths by Magnetically Induced Currents. *Phys. Chem. Chem. Phys.* **2011**, *13*, 434−437.
(37) Adam, W.; Grimison, A.; Hoffmann, R.; Zuazaga de Ortiz, C. Hydrogen Bonding in Pyridine. *J. Am. Chem. Soc.* **1968**, *90*, 1509−1516.
(38) Herskovits, T. T.; Harrington, J. P. Solution Studies of the Nucleic Acid Bases and Related Model Compounds. Solubility in Aqueous Alcohol and Glycol Solutions. *Biochemistry* **1972**, *11*, 4800−4811.
(39) Dračínský, M. The Chemical Bond: The Perspective of NMR Spectroscopy. *Annual Reports on NMR Spectroscopy*, 2017; Vol. *90*, pp 1−40.
(40) Pogorzelski, S. J.; Kogut, A. D. Static and Dynamic Properties of Surfactant Films on Natural Waters. *Oceanologia* **2001**, *43*, 223−246.
(41) Zhou, N. F.; Pethica, B. A. Monolayers of Human Plasma Fibronectin at the Air/Water Interface. *Langmuir* **1986**, *2*, 47−50.

https://dx.doi.org/10.1021/acsomega.0c02147
ACS Omega 2020, 5, 21538−21549

(42) Bal, J. K.; Kundu, S.; Hazra, S. Hydrophobic to Hydrophilic Transition of HF-Treated Si Surface during Langmuir−Blodgett Film Deposition. *Chem. Phys. Lett.* **2010**, *500*, 90−95.
(43) Vignaud, G.; Chebil, M. S.; Bal, J. K.; Delorme, N.; Beuvier, T.; Grohens, Y.; Gibaud, A. Densification and Depression in Glass Transition Temperature in Polystyrene Thin Films. *Langmuir* **2014**, *30*, 11599−11608.
(44) Bal, J. K.; Beuvier, T.; Unni, A. B.; Chavez Panduro, E. A.; Vignaud, G.; Delorme, N.; Chebil, M. S.; Grohens, Y.; Gibaud, A. Stability of Polymer Ultrathin Films (<7 Nm) Made by a Top-Down Approach. *ACS Nano* **2015**, *9*, 8184−8193.
(45) Rebuffi, L.; Plaisier, J. R.; Abdellatief, M.; Lausi, A.; Scardi, P. Mcx: A Synchrotron Radiation Beamline for X-Ray Diffraction Line Profile Analysis. *Z. Anorg. Allg. Chem.* **2014**, *640*, 3100−3106.
(46) Daillant, J.; Gibaud, A. X-Ray and Neutron Reflectivity. *Lecture Notes in Physics*; Daillant, J., Gibaud, A., Eds.; Springer Berlin Heidelberg: Berlin, Heidelberg, 2009; Vol. *770*.
(47) Bal, J. K.; Beuvier, T.; Chebil, M. S.; Vignaud, G.; Grohens, Y.; Sanyal, M. K.; Gibaud, A. Relaxation of Ultrathin Polystyrene Films Hyperswollen in Supercritical Carbon Dioxide. *Macromolecules* **2014**, *47*, 8738−8747.
(48) Vignaud, G.; Gibaud, A. REFLEX : A Program for the Analysis of Specular X-Ray and Neutron Reflectivity Data. *J. Appl. Crystallogr.* **2019**, *52*, 201−213.

https://dx.doi.org/10.1021/acsomega.0c02147
ACS Omega 2020, 5, 21538−21549